

Magnetic Resonance Imaging of the Knee: An Overview and Update of Conventional and State of the Art Imaging

Nicholas C. Nacey, MD, Matthew G. Geeslin, MD, Grady Wilson Miller, PhD, and
Jennifer L. Pierce, MD*

CME

This article is accredited as a journal-based CME activity. If you wish to receive credit for this activity, please refer to the website: www.wileyhealthlearning.com/jmri

ACCREDITATION AND DESIGNATION STATEMENT

Blackwell Futura Media Services designates this journal based CME activity for a maximum of 1 *AMA PRA Category 1 Credit*TM. Physicians should only claim credit commensurate with the extent of their participation in the activity.

Blackwell Futura Media Services is accredited by the Accreditation Council for Continuing Medical Education to provide continuing medical education for physicians.

EDUCATIONAL OBJECTIVES

Upon completion of this educational activity, participants will be better able to:

Understand and apply the basic and state of the art MR sequences for diagnosing pathology of the knee.

ACTIVITY DISCLOSURES

No commercial support has been accepted related to the development or publication of this activity.

Faculty Disclosures:

Editor-in-Chief: Mark E. Schweitzer, MD, has no relevant financial relationships to disclose.

CME Editor: Mustafa R. Bashir, MD, discloses research support from Siemens Healthcare and GE Healthcare.

CME Committee:

Nicoletta Anzalone, MD, has no relevant financial relationships to disclose.

Eric Chang, MD, has no relevant financial relationships to disclose.

Bonnie Joe, MD, PhD, has no relevant financial relationships to disclose.

Tim Leiner, MD, PhD, has no relevant financial relationships to disclose.

Bruno Madore, PhD, has no relevant financial relationships to disclose.

Shreyas Vasanaawala, MD, PhD, discloses research support from GE Healthcare, and founder's equity in Arterys.

Authors:

Nicholas C Nacey, Matthew G. Geeslin, Grady Wilson Miller, and Jennifer L. Pierce, have no relevant financial relationships to disclose.

This manuscript underwent peer review in line with the standards of editorial integrity and publication ethics maintained by Journal of Magnetic Resonance Imaging. The peer reviewers have no relevant financial relationships. The peer review process for Journal of Magnetic Resonance Imaging is double-blinded. As such, the identities of the reviewers are not disclosed in line with the standard accepted practices of medical journal peer review.

Conflicts of interest have been identified and resolved in accordance with Blackwell Futura Media Services' Policy on Activity Disclosure and Conflict of Interest.

INSTRUCTIONS ON RECEIVING CREDIT

For information on applicability and acceptance of CME credit for this activity, please consult your professional licensing board.

This activity is designed to be completed within an hour; physicians should claim only those credits that reflect the time actually spent in the activity. To successfully earn credit, participants must complete the activity during the valid credit period.

Follow these steps to earn credit:

- Log on to www.wileyhealthlearning.com/jmri
- Read the target audience, educational objectives, and activity disclosures.
- Read the article in print or online format.
- Reflect on the article.
- Access the CME Exam, and choose the best answer to each question.
- Complete the required evaluation component of the activity.

This activity will be available for CME credit for twelve months following its publication date. At that time, it will be reviewed and potentially updated and extended for an additional period.

View this article online at wileyonlinelibrary.com. DOI: 10.1002/jmri.25620

Received Jul 2, 2016, Accepted for publication Nov 4, 2016.

*Address reprint requests to: J.L.P., Department of Radiology and Medical Imaging, University of Virginia, 1215 Lee St., Charlottesville, VA 22908.

E-mail: jpierce@virginia.edu

From the and Department of Radiology and Medical Imaging, University of Virginia, Charlottesville, Virginia, USA

Magnetic resonance imaging (MRI) has become the preferred modality for imaging the knee to show pathology and guide patient management and treatment. The knee is one of the most frequently injured joints, and knee pain is a pervasive difficulty that can affect all age groups. Due to the diverse pathology, complex anatomy, and a myriad of injury mechanisms of the knee, the MRI knee protocol and sequences should ensure detection of both soft tissue and osseous structures in detail and with accuracy. The knowledge of knee anatomy and the normal or injured MRI appearance of these key structures are critical for precise diagnosis. Advances in MRI technology provide the imaging necessary to obtain high-resolution images to evaluate menisci, ligaments, and tendons. Furthermore, recent advances in MRI techniques allow for improved imaging in the postoperative knee and metal artifact reduction, tumor imaging, cartilage evaluation, and visualization of nerves. As treatment and operative management techniques evolve, understanding the correct application of these advancements in MRI of the knee will prove to be valuable to clinical practice.

Level of Evidence: 5

J. MAGN. RESON. IMAGING 2017;45:1257–1275

Although a great deal of clinical information can be obtained from a patient's history and physical exam, magnetic resonance imaging (MRI) has become integral for the diagnosis and treatment planning of knee pathology. However, many times the physical exam is difficult and unclear. The superior ability to detect soft tissue and osseous injuries confirms that MR is the most comprehensive modality for imaging the knee. This article discusses pathology of the knee and outlines the application of the technical aspects of high-resolution MRI of the knee. The diagnostic criteria of detecting meniscal and cruciate tears with MRI is reviewed. An update on knee MRI pertaining to advanced imaging of postoperative menisci, metal artifact reduction and knee arthroplasty, tumors, cartilage, nerves, joint inflammation, and 3D isotropic and ultrashort echo time (TE) sequences are presented (Table 1).

Meniscus

With meniscal tear detection rates of accuracy, sensitivity, and specificity ranging from 85–95%, MRI has become the preferred modality of imaging for visualizing and diagnosing meniscal pathology since its introduction into clinical practice in the 1980s.¹ The role of MRI has also expanded beyond just meniscal tear identification. The meniscal tear type, location, and extent are all critical imaging findings that MR provides that affect surgical technique and guide patient management.

In the absence of prior surgery, a meniscal tear is diagnosed on MR by increased intrasubstance signal unequivocally breaching the articular surface and/or changes to the meniscal shape or size.² If the signal is seen on two slices with a 3-mm slice thickness, the positive predictive value for a tear is 94% in the medial meniscus and 96% in the lateral meniscus. These two slices can be contiguous images or from one coronal and one sagittal image.^{2–4} When the meniscal signal or morphological abnormality is seen only on a single image, the positive predictive value significantly decreases to 43% and 18% for medial and lateral meniscal tears, respectively.³ These are reported as possible tears at our institution.

The meniscal tear patterns include: horizontal, longitudinal vertical, radial, vertical/horizontal flap, and complex (combination of horizontal, vertical, and radial) tears. Horizontal tears and radial tears typically require debridement.⁵

When they occur in the peripheral vascular “red-zone” of the meniscus, longitudinal vertical tears are often treated with surgical repair.

Horizontal Tears

Horizontal tears run parallel to the tibial articular surface and divide the meniscus into upper and lower parts. These tears are most often degenerative and associated with parameniscal cyst formation secondary to joint fluid infiltrating the two components of the tear. The presence of a parameniscal cyst has a positive predictive value greater than 90% for meniscal tear, unless the cyst is located along the anterior horn. When parameniscal cysts are located along the anterior horn of the lateral meniscus, there is a tear in 64% of cases.⁶

Longitudinal Vertical Tears

Longitudinal vertical tears run perpendicular to the tibial articular surface and divide the meniscus into inner and outer parts. These tears are typically seen in relatively young patients after a traumatic event. There is a strong association of these meniscal tears with anterior cruciate ligament (ACL) injury such that 90% of medial and 83% of lateral peripheral longitudinal vertical tears are present with concomitant ACL tears.³ Also, longitudinal vertical tears are the most common type of meniscal tears that will displace and produce a bucket handle tear, where the inner segment moves centrally or migrates any direction away from the tear. This displacement produces the well-known indirect signs of a bucket handle tear like the double posterior cruciate ligament (PCL) and double anterior horn signs.

Radial Tears

Radial tears involve the inner margin or free edge of the meniscus and run straight into the meniscus both perpendicular and parallel to the tibial articular surface. These tears produce anterior and posterior parts, causing significant loss of meniscal function because of the disruption of the circumferential fibers of the meniscus and degrading the ability of the meniscus to resist hoop stress. Radial tears should be further described by detailing the depth of meniscal involvement as partial or complete. If the radial tear is complete by involving the inner margin and extending out into the

TABLE 1. Knee MRI Protocols

	Sag FSE PD (2.5mm)	Sag FSE PD fat sat	Cor FSE PD	Cor FSE T2 fat sat	Ax FSE T2 fat sat	
Knee arthrogram	Sag T1 fat sat	Sag FSE T2	Cor T1 fat sat	Cor STIR	Ax T1	
Knee metal reduction	Sag STIR	Sag PD	Cor STIR	Cor PD	Ax STIR	Double bandwidth and echotrain length
Knee tumor	Sag T1 fat sat	Sag STIR	Cor T1	Cor STIR	Ax STIR	Ax T1 fat sat pre
Knee synovitis/ infection	Sag STIR	Sag T1	Cor STIR	Ax T1	Ax STIR	Ax T1 fat sat post

periphery of the meniscus, the gap or region of meniscal discontinuity should be measured and reported. Because these tears involve the inner, avascular region of the meniscus, radial tears do not heal or regain function after surgery, and are thus treated with surgical debridement.⁷ Radial tears frequently occur in the posterior horn of the medial meniscus or the anterior horn and body junction of the lateral meniscus.³ Radial tears involving the posterior horn root ligaments of the menisci are important to recognize on preoperative MRI since standard arthroscopy portal placement does not adequately visualize this area. Prior knowledge of this type of tear is necessary to plan for the required additional portals for treatment.³

Radial tears have a variable appearance and can be seen best on both sagittal and coronal planes, depending on the location of the tear relative to the plane of imaging. When utilizing image slice thicknesses of 3 mm or less, radial tears can also be assessed on axial planes. A radial tear in the body segment will appear like a cleft in the sagittal plane because it is imaged perpendicular to the tear (Fig. 1a). This same tear would appear like a truncated or blunted meniscus (Fig. 1b) in the coronal plane (in-plane to the tear).

Vertical and Horizontal Flap Tears

Vertical and horizontal flap tears are produced when portions of torn menisci become displaced. These tears can be comprised of vertical, horizontal, and radial tear components. These are unstable injuries and preoperative diagnosis with MRI is critical to provide the surgeon with the location of the displacement. If the torn and displaced meniscus extends into the joint recesses like the medial or lateral gutters, arthroscopy does not directly visualize these regions. Only when made aware of this finding by MRI can proper surgical technique of probing and hooking be performed to release the displaced fragment. The medial meniscus is involved 6–7 times more in vertical tears than the lateral meniscus. The displaced flap tears can be frequently seen along the posterior joint near the PCL (two-thirds of cases) and the medial/lateral gutters.⁸ When a blunted or diminutive meniscus is encountered, a thorough evaluation for a displaced fragment in the joint recesses or intercondylar notch should be performed.

Meniscal Root Tears

The roots of the menisci overlie the tibial spines and then insert onto the tibia, very close to the PCL (Fig. 2a). Therefore, if the meniscal roots are not seen on sagittal images immediately adjacent to the PCL (Fig. 2b), a root tear should be expected especially for the medial posterior root ligament. More than the sagittal plane, coronal fluid sensitive sequences better delineate the roots of the menisci from the tibial spines and PCL (Fig. 2c).⁹

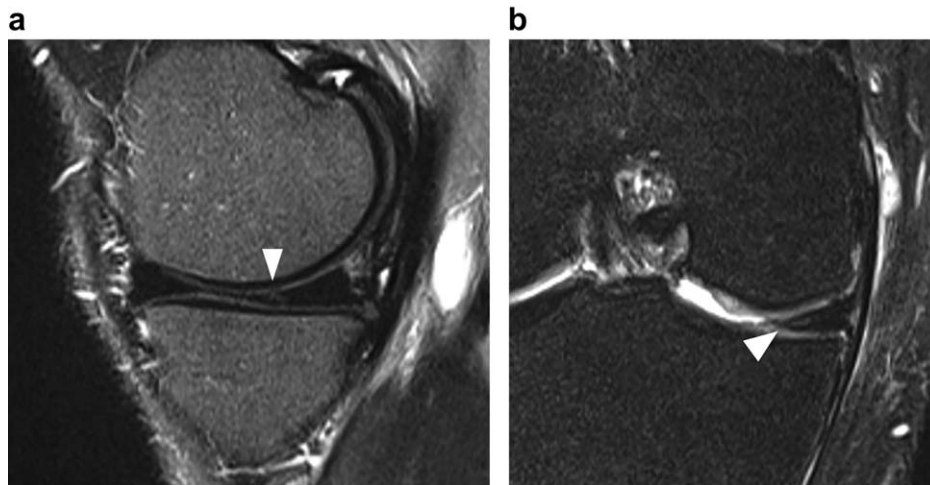


FIGURE 1: A sagittal PD-weighted (TR/TE: 4000/30 msec) image (a) demonstrates a cleft in the body/posterior horn junction of the medial meniscus due to a radial tear that is oriented perpendicular to the plane of imaging. In the coronal plane the tear is in-plane to the tear. Thus, a T_2 -weighted (TR/TE: 6300/78 msec) fat-suppressed image (b) shows the same radial tear as blunting and signal change of the free edge or inner margin of the meniscus.

MRI Parameters for Meniscal Tears

Short echo time (TE) or proton density (PD)-weighted sequences have historically been favored over T_2 -weighted sequences for the detection of meniscal tears (Nguyen). However, T_2 -weighted sequences demonstrate higher accuracy for the detection of meniscal tears at the meniscocapsular junction and roots.^{2,3,10} Increasing matrix size and decreasing field of view and slice thickness increase spatial resolution to aid in the evaluation of the meniscus. At our institution, a field of view of 16 cm is used along with a matrix of 320×320 and a slice thickness of 3 mm. Utilizing PD sequences without fat suppression provides more signal to even decrease the slice thickness to less than 3 mm, especially on higher-strength magnets (3T) or with increasing the number of acquisitions. At our institution, fast spin echo (FSE) sequences are performed. These faster FSE sequences are optimized with echo train length less than five

and longer bandwidths and have been found to have no statistical difference in tear detection rate when compared with longer conventional spin-echo techniques.²

3D sequences with isotropic resolution reduces partial volume averaging, provides thinner slices, and produces faster imaging of the knee with the ability to create multiplanar reformations after just a single plane acquisition.² Although the early comparisons of 3D and the standard 2D techniques have shown no significant difference in meniscal tear detection,¹¹ more research and evaluation is needed, and our institution continues to utilize the high spatial resolution of the 2D FSE sequences.

Cruciates

Anterior Cruciate Ligament

The most commonly injured major ligament of the knee is the ACL. The ACL stabilizes the knee by resisting anterior



FIGURE 2: A coronal PD-weighted (TR/TE: 400/38 msec) image (a) demonstrates the close location and relationship of the posterior meniscal roots and the PCL. A sagittal PD-weighted (TR/TE: 4000/33 msec) image (b) shows that the posterior horn medial meniscal root is especially located adjacent to the PCL. The meniscal roots are best visualized in a coronal plane as seen on a T_2 -weighted (5000/84 msec) fat-suppressed image (c) showing the tear and gap defect of the posterior horn medial meniscal root.

translation, rotatory load, and restraint of varus and valgus forces. MRI is highly accurate for full-thickness ACL tears with a sensitivity of 83–95% and specificity of 95–100%.¹² Due to magic angle artifact and the oblique course of the ACL fibers, T_2 -weighted sequences are recommended over T_1 -weighted sequences for the evaluation of the ACL. In the sagittal plane, the normal ACL fibers are taut and parallel to the roof of the intercondylar notch. The primary MRI sign for complete ACL tears is fiber discontinuity, which is best visualized in the sagittal and axial images.¹³ However, when interpreting MR images of the knee it is important to evaluate all the planes for ACL tears, including the coronal plane. Also in the sagittal plane, a wavy appearance and a horizontal orientation of the ACL, such that an angle of less than 45° between the distal ACL and the tibia, are highly accurate secondary MRI signs and findings of complete tears of the ACL.¹²

Several bone contusions and marrow edema signal changes have been reported as secondary MRI signs of an ACL tear. Osseous injuries due to the anterior translation of the tibia and impaction onto the femur have been described that include pivot-shift bone contusions involving the anterior/central lateral femoral condyle and the posterior lateral tibial plateau, countercoup bone contusion of the posteromedial tibial plateau, and Segond avulsion fractures involving the anterolateral ligament and lateral capsular structures. These osseous contusions are best depicted on fat-suppressed fluid sensitive sequences (T_2 -weighted sequence with fat suppression or STIR). It is important to recognize these osseous injuries due to the increased incidence of meniscal tears and a relatively poor clinical outcome at 1 year after ACL reconstruction.¹³

Of all ACL tears, 30% are partial tears of the ACL involving the anteromedial or posterolateral bundles.¹⁴ The anteromedial bundle is maximally taut and resists anterior translation of the tibia during knee flexion. The posteromedial bundle is maximally taut and prevents anterior translation in extension and internal rotation.¹² Tear of the anteromedial bundle with a normal or partial tear of the posterolateral bundle is the most common pattern of partial ACL tears.^{12,15} Tears of the anteromedial bundle are three times more than posteromedial bundle tears.¹⁶ In contrast to complete ACL tears, MRI for identifying partial tears is significantly more difficult, with sensitivity of 62–81%, specificity of 19–97%, and accuracy rates of 25–53%.¹² New imaging planes have been suggested for better visualization of the two bundle, which improves the diagnosis of partial ACL tears. 3T MR images in the oblique coronal plane (oriented along the longitudinal axis of the ACL or the roof of the intercondylar notch) yielded significantly greater specificity at 92–96% for selective bundle tears, whereas conventional sagittal and coronal planes yielded a specificity of 67% (Fig. 3).¹⁶ The use of this imaging plane can be beneficial, as



FIGURE 3: An oblique coronal PD-weighted (TR/TE: 4000/28 msec) image was obtained with the plane of imaging oriented along the longitudinal axis of the ACL. This demonstrates clear delineation of the anteromedial bundle of the ACL.

more selective ACL bundle or double bundle ACL reconstructions are performed. Of note, 3D isotropic FSE acquisitions can produce high-quality multiplanar reformatted images in multiple oblique planes to evaluate the ACL; however, they demonstrate similar diagnostic performance to the standard 2D sequences in the conventional planes.^{12,17}

Posterior Cruciate Ligament

PCL tears account for 3% of all knee injuries.^{12,18} The most common mechanism of injury of the PCL is the dashboard injury, where the anterior force onto the proximal tibia causes posterior translation. Because of this high-energy mechanism, PCL tears are more commonly associated with multiligamentous injuries. Isolated PCL tears are not common.¹² In the athletic population, injuries related to hyperflexion and hyperextension can be a cause of PCL rupture. The PCL is usually less than 6 mm in anterior–posterior dimension and diffusely low signal intensity on all sequences.¹⁸ The PCL is unusual in that the fibers most often do not frankly disrupt with tearing. Instead, the ligament stretches significantly and becomes structurally incompetent.¹⁸ On MRI, a thickened PCL, complete intrasubstance tears, and avulsions indicate PCL tearing. On MRI, a thickened PCL of more than 7 mm is highly suspicious for a tear, with a sensitivity of 94% and specificity of 92%.¹⁸ Furthermore, the intrasubstance signal abnormality with the PCL is better seen on the T_1 or PD sequences. Less frequently is there increased T_2 -weighted/fluid signal in PCL tears.^{12,18} Due to these imaging features, the diagnosis of PCL tears may be missed.

Postoperative Change / MR Arthrography

Special protocol considerations may be necessary in the case of prior meniscus surgery, whether the prior surgery be meniscectomy (resection of a portion of the torn meniscal

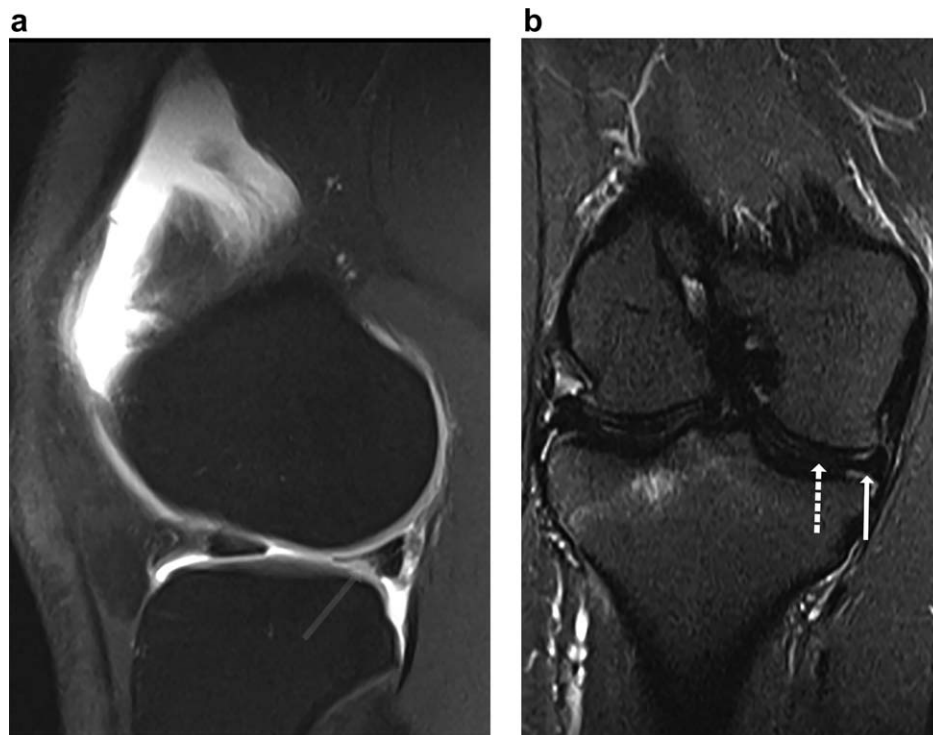


FIGURE 4: A sagittal T_1 -weighted (TR/TE: 545/11 msec) fat-suppressed image performed after the administration of 30 cc of intra-articular gadolinium (a) demonstrates hyperintense gadolinium tracking into the blunted meniscus, consistent with a recurrent tear. One can alternatively utilize fluid signal intensity on a T_2 -weighted image as evidence of a meniscal tear; however, the use of STIR images should be avoided as demonstrated by this coronal STIR (TR/TE/TI: 4510/51/150 msec) image from an MR arthrogram (b), which shows hypointense joint fluid due to suppression of gadolinium signal preventing differentiation of fluid from meniscal tissue. T_2 -weighted images with chemical fat suppression should be utilized if an MR arthrogram is performed.

tissue), repair (suturing of torn meniscus with the goal of eventual healing in the vascularized meniscal periphery), or transplantation (typically cadaveric allograft implantation with bone plugs in cases of extensive meniscal pathology). Following prior meniscal surgery, the typical criteria for diagnosing meniscal tears in the native knee including abnormal meniscus morphology and linear signal contacting a meniscal surface on two images may no longer hold true. The meniscus may take on a blunted appearance, particularly in the free edge, following meniscectomy. Linear signal on intermediate weighted sequences (such as proton density) contacting a meniscal surface is a nonspecific finding that may indicate a recurrent tear in an area of prior meniscal surgery, residual degenerative or healed meniscal signal at the margin of resection, or healed meniscal tissue at the site of prior repair.¹⁹ Other findings such as displaced meniscal tissue, a parameniscal cyst, or typical findings of a tear in a nonoperated portion of the meniscus can still be utilized as specific but insensitive indicators of a postoperative meniscal tear. Correlation with the operative report and prior imaging is critical when interpreting postoperative menisci MRI; the timing, location, type of meniscal surgery, and amount of meniscal tissue removed is all critical information.

Knee arthrography has been utilized as a tool in evaluating the postoperative meniscus. Arthrography distends the

joint, and T_1 -weighted fat-suppressed images can demonstrate contrast tracking into a meniscal reter (Fig. 4a). The primary downside of arthrography is the necessity of an interventional procedure preceding the MRI exam, typically performed under fluoroscopy or ultrasound. Gadolinium is diluted to a 1:200 concentration with saline. The saline can be partially substituted with an anesthetic and/or steroids without decreasing the quality of the MR signal.²⁰ At least 30 cc is utilized for knee arthrography compared to 10–12 cc for the shoulder or hip. Indirect arthrography, the injection of intravenous gadolinium before imaging to make a tear more apparent, has also been evaluated for evaluation of the postoperative meniscus and has not been found to have any improved accuracy over conventional MRI or direct arthrography, likely because the fibrovascular tissue in healed meniscal tears can enhance, as can a true tear.²¹

T_2 -weighted fluid sensitive images are an important component of postsurgical meniscal evaluation. Fluid signal tracking into the meniscus on T_2 -weighted imaging has also been reported as a specific, but not necessarily sensitive indicator of a meniscal reter in postsurgical patients.²¹ The presence of a joint effusion may provide a natural arthrographic effect even if direct arthrography is not performed, which can promote the extension of fluid into a discrete meniscal reter.²² If T_2 -weighted images are being performed as part

of a direct arthrogram, the use of T_2 -weighted fat-suppressed images is preferable for this purpose, as STIR images will show suppression of both fat and intraarticular gadolinium (Fig. 4b).

The utility of arthrography compared to conventional MRI has been extensively debated in the literature. In a 2003 study, Magee et al found that arthrography was most beneficial for patients who have had prior meniscal repair or meniscectomy involving greater than 25% of the meniscus, while patients who had less than 25% of the meniscus resected could undergo conventional MRI.²³ In patients where less than 25% of the meniscus has been resected, the same criteria can be used as when evaluating the native meniscus.²⁴ Some have suggested obtaining MR images before and after performing arthrography, as the increased T_1 signal in a return meniscus may not always be as bright as that as the gadolinium within the joint, thus obtaining precontrast images may help increase accuracy for retreating.²⁵ However, this approach may not be appropriate for some practices, as it is more time-consuming and difficult to schedule. Other groups will either perform arthrography in all patients with prior meniscus surgery, or perform conventional MRI in all cases and reserve arthrography only for problematic cases.²⁶

Tumor Imaging of the KNEE

Radiographs should still be considered the initial step in imaging of musculoskeletal tumors; however, MRI is generally required for further lesion characterization. Musculoskeletal tumor imaging within the knee employs the same MRI techniques as the rest of the musculoskeletal system. These techniques can be grouped by three general aims: initial lesion characterization, assessing pretreatment extent of disease, and posttreatment evaluation of treatment response and surveillance for recurrence. Lesions characterized as indeterminate or malignant will proceed to tissue sampling; only those with convincing imaging findings of a specific benign diagnosis can avoid biopsy. If tissue sampling is performed and primary bone malignancy is diagnosed, the ipsilateral joint above and below the lesion must be imaged to evaluate for skip lesions. The MRI methods presently used for tumor imaging include anatomic, functional, and metabolic MRI.²⁷ Conventional anatomic imaging is generally adequate for delineating the extent of tumor involvement and invasion of nearby structures such as the neurovascular bundle. Advanced techniques such as chemical shift imaging, diffusion-weighted imaging, MR perfusion, and MR spectroscopy can be employed if desired, albeit at the expense of a longer imaging time and potential lack of availability at all institutions.

Conventional anatomic sequences consisting of T_1 -weighted, STIR or T_2 -weighted fat-suppressed, and T_1 -weighted postcontrast images serve as the traditional means

of tumor evaluation in the musculoskeletal system. T_1 -weighted imaging is particularly useful for bone lesions, as the hyperintense signal from yellow marrow contrasts with the T_1 hypointensity typical of most bone tumors.²⁸ Contrast between most soft-tissue masses and muscle is more limited on T_1 -weighted imaging, thus T_2 -weighted images, either STIR or T_2 -weighted fat-suppressed, are more helpful for delineating a soft-tissue mass.²⁷ Most areas of tumor recurrence will demonstrate mass-like T_2 hyperintensity,²⁹ although this depends on the presurgical imaging characteristics of the tumor. Contrast should be given for any knee mass that is not clearly a ganglion or Baker's cyst, as many tumors have T_2 hyperintense components from myxoid tissue deposition that can mimic fluid within a cyst (Fig. 5a). Parameters such as TR/TE and fat suppression should be kept consistent on pre- and postcontrast imaging, as the failure to do so can result in signal intensity changes that can be mistaken for enhancement. A fat-suppressed precontrast image should be added to the protocol if all postcontrast imaging is fat saturated (Fig. 5b,c).

Advanced imaging techniques include chemical shift imaging, diffusion-weighted imaging, MR perfusion, and MR spectroscopy. These techniques have yet to find widespread clinical utilization, although they may be helpful for troubleshooting particular situations or for routine tumor imaging at some select institutions. Chemical shift imaging compares the signal intensity of in-phase to opposed-phase images to identify small areas of fat mixed with water in the same voxel, potentially allowing one to differentiate fatty marrow-replacing tumor from bone marrow edema and/or hematopoietic marrow in an otherwise nonspecific bone lesion.²⁷ A decrease in signal on the opposed-phase image by 20% or more relative to the in-phase image is suggestive of a benign etiology that is not replacing marrow fat.³⁰ Diffusion weighting with echo planar imaging takes advantage of the high cellularity within soft-tissue neoplasms, with a resulting hyperintense signal on diffusion-weighted images and hypointense signal on the apparent diffusion coefficient (ADC) map.³¹ A lower ADC correlates with a higher risk of malignancy in soft-tissue lesions.³² Diffusion-weighted imaging is most beneficial in cases where intravenous contrast cannot be administered or as an adjunct to gadolinium in postoperative cases to increase specificity over gadolinium images alone.^{33,34} MRI perfusion with dynamic contrast-enhanced imaging exploits the difference in enhancement patterns between malignant and benign lesions, wherein malignant lesions typically demonstrate rapid uptake of contrast.^{27,35,36} Perfusion imaging requires the rapid generation of high-resolution images, thus time-resolved MR angiography techniques such as TWIST are typically utilized,³¹ and the utilization of subtraction images can be considered.³⁷ Dynamic contrast-enhanced imaging may be of particular

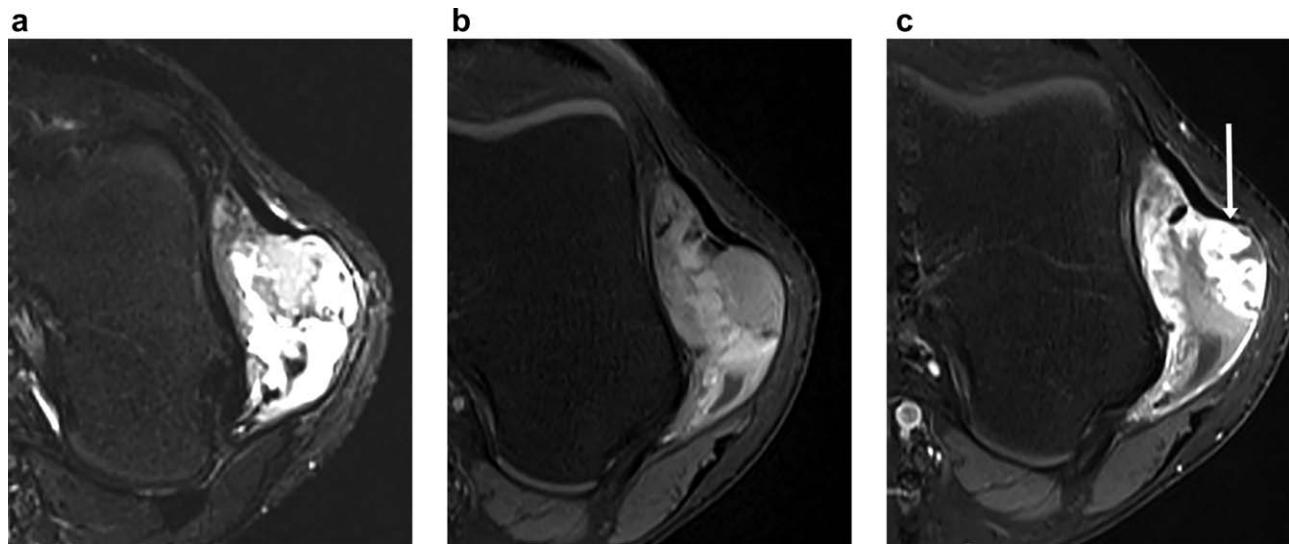


FIGURE 5: An axial STIR (TR/TE/TI: 6454/41/220 msec) image (a) demonstrates a markedly T_2 hyperintense mass along the lateral aspect of the distal femur. While ganglia can appear as T_2 hyperintense, a mass was suspected given the atypical location for a ganglion and heterogenous appearance. A precontrast T_1 -weighted (TR/TE: 843/16 msec) fat-saturated image (b) demonstrates internal complexity of the mass with some T_1 hyperintense components, and thus provides a useful baseline for measuring enhancement. On the subsequent postcontrast image (c) obtained with the same imaging parameters, superimposed enhancement is seen within the lesion (solid arrow), which was eventually biopsied and found to be a synovial sarcoma.

benefit in the follow-up of soft-tissue sarcomas after treatment, with a recent study showing a 97% specificity for recurrent tumor compared to 52% for conventional post-contrast images.³³ MR spectroscopy assesses the chemical composition of tissue, with a higher percentage of choline suggestive of malignancy due to an increased rate of phospholipid membrane turnover.³¹ Spectroscopy of musculoskeletal lesions is in its early stages of development, but has shown promise in being able to distinguish malignant from benign lesions.³⁸

Postarthroplasty/Metal Reduction

The metallic component of a total knee arthroplasty produces artifact from spin dephasing with both in-plane and through-plane distortion, which has traditionally limited the use of MRI. However, there are techniques available that can limit the artifact and produce images of diagnostic quality (Table 1), and ongoing research may yield new options for metal reduction or further improve upon existing techniques. While arthroplasty is the most dramatic example of an instance where metal artifact reduction techniques are necessary, patients with smaller amounts of metal such as interference screws or staples will also have improved images if such techniques are utilized.

The first step in reducing metal artifact is choosing the appropriate magnetic field strength, as higher field strength will worsen any metal artifact by increasing the size of the artifact-inducing magnetic field gradients. Fast spin echo sequences will result in less metal artifact than gradient echo images due to their use of refocusing pulses. Chemical fat saturation pulses result in extensive susceptibility artifact

and poor fat suppression (Fig. 6a), thus STIR sequences are preferred to obtain fluid sensitive images. Dixon techniques alternatively can suppress fat with less metal artifact than seen in chemical fat saturation images. Sequences with a shorter TE, such as T_1 - or PD-weighted sequences, will typically also demonstrate less artifact than sequences with a longer TE, thus PD sequences in particular are helpful, as they demonstrate fluid but produce minimal artifact.³⁹

Parameter choice can have a dramatic impact on reducing metal artifact. Increasing the readout bandwidth to greater than 500 Hz/pixel will decrease artifact.⁴⁰ The larger gradient amplitude associated with higher readout bandwidth reduces spatial distortion, by reducing the relative size of the metal-induced magnetic field gradients, while the shorter data sampling time enabled by the larger gradient amplitude reduces signal loss due to intravoxel dephasing in the presence of these background gradients. Factors that decrease voxel size such as either increasing the matrix, decreasing slice thickness, or decreasing the field of view will also reduce artifact by reducing intravoxel signal dephasing,^{41,42} albeit at the cost of decreased signal-to-noise ratio (SNR). Increasing the echo train length will also reduce metal artifact, albeit at the expense of lower SNR and image blurring.³⁹ The increased echo train length results in a shorter time between echoes of an FSE sequence, assuming a constant total echo duration, thus allowing for less spin dephasing and thereby less metal artifact. Swapping the phase encoding and frequency encoding directions will not necessarily reduce artifact, but may shift the artifact such that previously obscured regions are now visible.³⁹

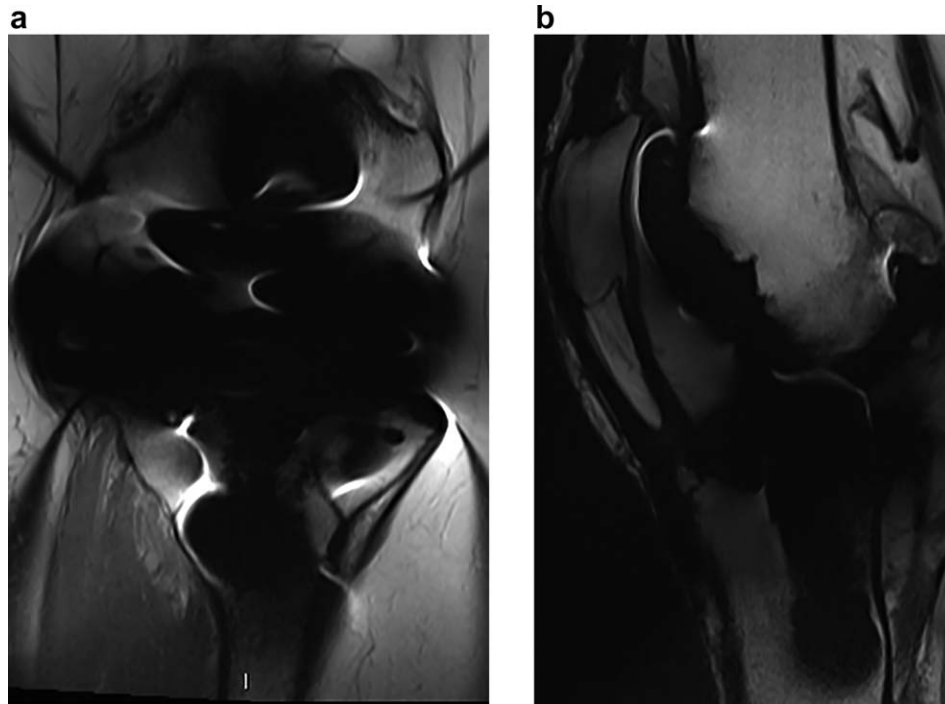


FIGURE 6: This coronal PD-weighted (TR/TE: 4000/23 msec) image (a) with fat saturation on a patient with a total knee arthroplasty has such extensive artifact that it cannot be used for diagnostic purposes. In contrast, a sagittal PD-weighted (TR/TE: 3000/38 msec) WARP (b) sequence (utilizing a high bandwidth and VAT) without fat suppression in a different patient with a total knee arthroplasty has some artifact but is of diagnostic quality.

Most clinical scanners now include specific metal artifact reduction (MARS) sequences that incorporate high bandwidth parameters. Some scanners also have more specialized packages that can help to further decrease metal artifact. View angle tilting (VAT) is a technique used to decrease in-plane distortion by adding a slice selection gradient during the readout period, which produces an effect as if the slice is being viewed from an angle, allowing the displacements in the slice selection and readout directions to cancel.³⁹ The WARP package (Fig. 6b) available on some scanners combines high bandwidth parameters with VAT.⁴² Slice encoding for metal artifact correction (SEMAC) is a package available on some scanners,⁴³ which adds phase-encoding steps to the slice selection direction to decrease artifact in the through-plane direction, which can be combined with the ability of VAT to decrease displacement of the in-plane dimension.³⁹ The multiacquisition variable-resonance image combination (MAVRIC) package available on some machines⁴³ uses spectrally overlapping 3D acquisitions to decrease the encoding errors typically seen with metal artifact.⁴⁴ The primary downside of both SEMAC and MAVRIC is the prolonged imaging time required, typically around 10 minutes per sequence.

Advanced Cartilage Imaging

Conventional 2D sequences can obtain adequate images of knee cartilage; however, these sequences are often chosen to

assess other structures in the knee such as menisci and ligaments. Dedicated cartilage sequences can provide a higher level of detail for cases where the cartilage is the primary concern, and has been an area of intensive ongoing research over the past decade. The two types of MR cartilage imaging are morphologic and compositional. Morphologic assessment of cartilage comprises a macroscopic evaluation of cartilage structure, with the intent to localize cartilaginous defects and fissures and quantify the area of the chondral surface involved as well as the depth of the defect (ie, "full thickness").⁴⁵ Resolution requirements to detect fissuring and fraying of cartilage are quoted at ~ 0.3 mm, in-plane.⁴⁶ In contrast, compositional assessment of cartilage aims to evaluate molecular status of the fluid-filled collagen and proteoglycan network comprising hyaline articular cartilage.⁴⁷ Compositional cartilage imaging includes techniques such as T_2 mapping, delayed gadolinium enhanced magnetic resonance imaging of cartilage (dGEMRIC), sodium ion imaging, $T_1\rho$ (T_1 rho) mapping, and diffusion-weighted imaging.⁴⁷⁻⁴⁹

Qualitative Techniques (SPACE, SPGR, DESS)

Sequences useful for morphologic cartilage evaluation include 3D FSE, 3D spoiled gradient echo (SPGR), and 3D dual-echo steady-state (DESS).⁵⁰ While these sequences can exquisitely demonstrate cartilage abnormalities, they do so at the expense of longer acquisition time relative to

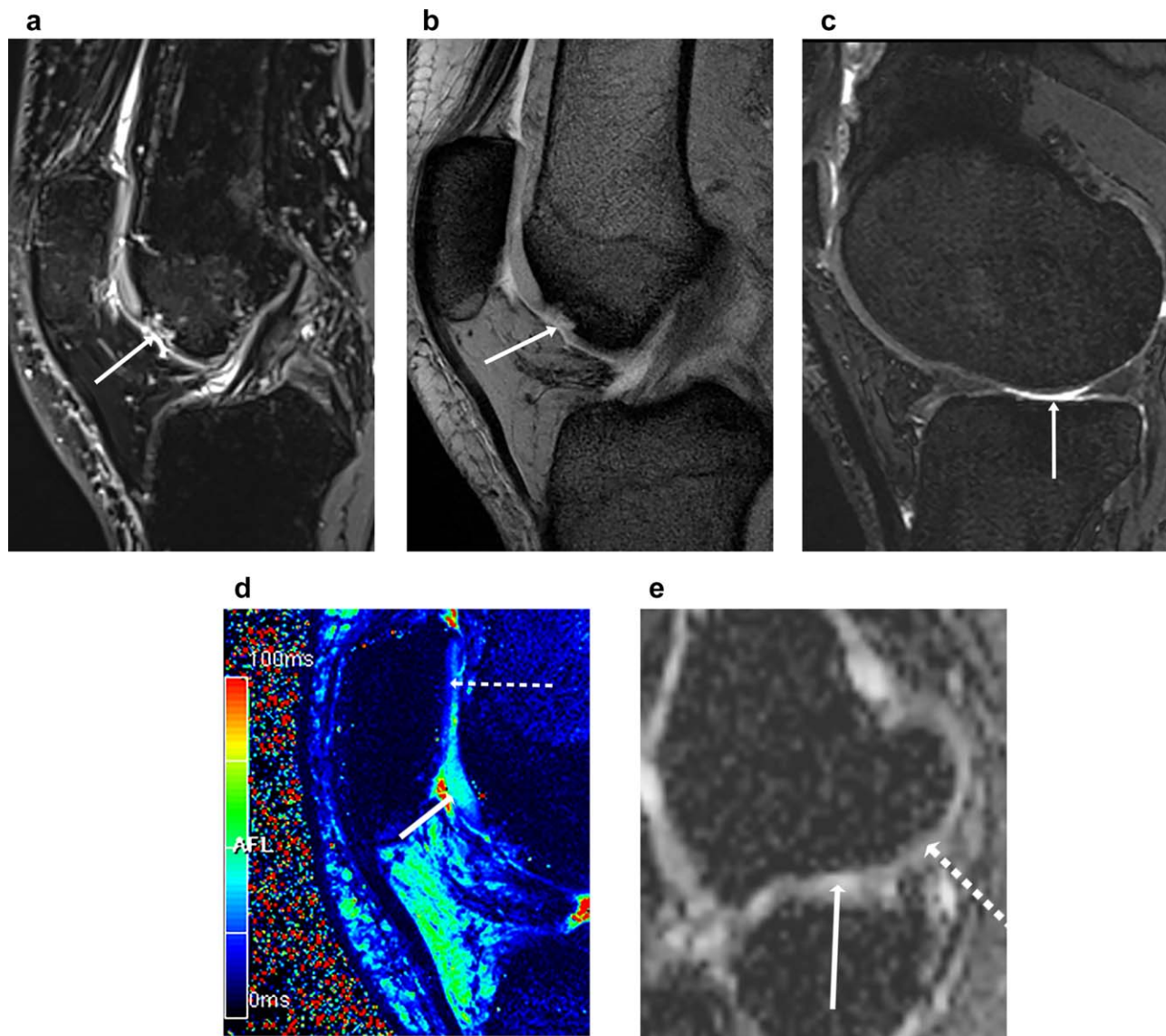


FIGURE 7: Advanced morphologic cartilage sequences including SPACE PD fat-suppressed, FLASH spoiled gradient echo, DESS, T_2 mapping, and diffusion-weighted imaging. A sagittal PD (TR/TE: 1200/28 msec) fat-suppressed SPACE image (a) clearly demonstrate a full thickness chondral defect in the lower trochlea with underlying subchondral marrow changes. A sagittal spoiled gradient echo FLASH (TR/TE: 600/10 msec, flip angle 25°) sagittal image (b) from the same patient also clearly demonstrates the trochlear cartilage defect, although the subchondral marrow changes are more difficult to visualize. A sagittal DESS (TR/TE: 14/5 msec, flip angle 60°) image from a different patient (c) shows high-grade chondral loss in the lateral tibial plateau. A sagittal T_2 mapping image (d) demonstrates prolonged T_2 in the superior trochlear cartilage (arrow) consistent with chondral degeneration, just superior to the same trochlear cartilage defect seen in image (b). Normal-appearing cartilage is noted in the patella (dashed arrow). The color scale for T_2 characteristics is present on the left side of the image. A sagittal ADC map (e) from a different patient (TR/TE 8800/107, $b = 0, 500, 1000 \text{ sec/mm}^2$) demonstrates hyperintense central within the central weight-bearing cartilage of the medial femoral condyle (straight arrow), while slightly darker signal is noted more posteriorly in the nonweight-bearing cartilage (dashed arrow). The more posterior cartilage demonstrates the expected signal within an area of intact cartilage due to restriction of diffusion, while the more central weight-bearing cartilage is abnormal and has lost the expected restricted diffusion, thus resulting in hyperintense signal.

conventional 2D sequences. 3D FSE acquisitions such as SPACE can be used to obtain variable contrasts that are helpful in cartilage evaluation, with proton density fat-saturated images being particularly beneficial for cartilage evaluation (Fig. 7a). 3D acquisitions avoid slice gaps and partial volume effects inherent to 2D acquisitions, and have the potential to decrease overall imaging time with the use

of multiplanar reconstruction. 3D FSE techniques have demonstrated diagnostic accuracy similar to that of 2D FSE techniques.^{46,51} The 3D SPGR sequence, sometimes referred to as FLASH, is available for clinical use on many MRI systems.^{47,52} The main limitation of SPGR is the decreased contrast (compared to T_2 or proton density) between joint fluid and articular cartilage, which somewhat

limits its sensitivity for surface defects.⁵³ 3D spoiled GRE sequences have been used for quantifying the thickness of articular cartilage (Fig. 7b); however, they are limited in their ability to assess subchondral bone for secondary findings of cartilage damage such as marrow edema.⁴⁶ The 3D DESS sequence employs two (or more) separate gradient echoes, which are then combined to increase SNR. The tissue contrast of the DESS sequence is unique in that fluid and cartilage demonstrate high signal, whereas trabecular bone is low in signal (Fig. 7c). 3D DESS acquisitions are more rapid than 3D SPGR, thereby decreasing sensitivity to motion. The high signal intensity of cartilage somewhat limits intra-substance cartilage evaluation, but 3D DESS has been shown to have accuracy similar to 2D and 3D GRE for the detection of articular cartilage lesions.⁴⁶ Of greatest utility in weight-bearing regions, an additional unique feature of 3D DESS is the ability to calculate articular cartilage volume.⁵³

T₂ Mapping

T_2 mapping produces quantitative T_2 measurement over a sampled region (in this case cartilage) and is depicted by a color overlay upon the tissue region of interest. The T_2 value is very sensitive to the hydration status of tissue, and the hydration status of tissue is reflective of the collagen concentration.⁵⁴ T_2 mapping is useful in detecting early disruption of the collagen matrix within articular cartilage, as this disruption leads to increased water content and commensurately higher T_2 values (Fig. 7d), when compared to normal cartilage.⁵⁵ T_2^* mapping provides more rapid acquisitions than T_2 mapping and has the potential for superior spatial resolution; however, is limited by greater sensitivity to magnetic field inhomogeneity, as may be found in the postsurgical setting.⁴⁹

dGEMRIC

dGEMRIC takes advantage of the charged ionic environment within cartilage, particularly that of glycosaminoglycans (GAGs), which are negatively charged.⁴⁸ The distribution of GAGs mirrors that of proteoglycans, and thus intact cartilage. dGEMRIC employs a negatively charged gadolinium contrast agent (GD-DTPA²⁻) which distributes preferentially to regions with lower GAG concentration, secondary to electrostatic repulsion.⁵³ A T_1 map of cartilage is obtained and scaled to reflect the distribution of gadolinium contrast, and thereby the regional distribution of intact (increased GAG concentration) and degenerated (decreased GAG concentration) cartilage. A logistical challenge of dGEMRIC is the required 90-minute interval between contrast injection and imaging. Conversely, positively charged sodium ions are attracted to negatively charged GAGs in intact cartilage.^{47,48}

Sodium Imaging

Similar to dGEMRIC, sodium imaging is based on the principle of negatively charged GAGs within intact cartilage. However, in the case of sodium imaging the positively charged ions are attracted to the negatively charged ions in intact cartilage. Sodium has a net nuclear magnetization and thus can be imaged by MRI⁵⁶; however, the concentration of sodium in the body is low, such that there is significantly less signal with sodium imaging compared to standard ¹HMRI, thus necessitating the use of 7T magnets to overcome this limitation. The lack of 7T magnet availability for clinical use has thus made sodium imaging largely impractical currently for patient care.

T₁ρ Mapping

The extracellular matrix of normal intact hyaline articular cartilage restricts the motion of water molecules. It follows that water molecules have greater mobility in damaged cartilage. This principle is utilized for $T_{1\rho}$ mapping of cartilage.⁴⁷ $T_{1\rho}$ is a relaxation time constant that differs from T_1 and T_2 , and it can be measured within cartilage using a specific pulse sequence. Generally, the length of relaxation time constants are as follows: $T_2 < T_{1\rho} < T_1$.⁵⁷ The value of the $T_{1\rho}$ time constant varies with the mobility of water within tissue and thus varies among intact and degenerating cartilaginous extracellular matrices.⁵⁸ Once sampled, $T_{1\rho}$ values can be mapped (just like T_2 and T_2^*) and displayed with an indexed color overlay to depict their relative values, and thereby the integrity of articular cartilage.⁵³ $T_{1\rho}$ imaging is a feasible technique for compositional cartilage imaging and is thought to have greater sensitivity⁵⁹ to early cartilage degeneration than other compositional techniques.⁵⁸

Diffusion-Weighted Imaging

Diffusion-weighted imaging is an intuitive application for compositional cartilage evaluation that evaluates for altered diffusion time within cartilage. In healthy cartilage, diffusion of water is restricted (ie, diffusion time is increased), resulting in a low ADC. In damaged cartilage, water is more mobile, resulting in decreased diffusion times and increased ADC values.^{47,60} The ADC values can then be mapped over articular cartilage, with the results delineating damaged and healthy cartilage (Fig. 7e).

Neurography

MR neurography of the knee is an uncommonly requested exam in most practices; however, there are unique anatomical and protocoling considerations when such a request is made. The sciatic nerve branches into the tibial nerve and common peroneal nerve typically in the superior aspect of the popliteal fossa.⁶¹ The common peroneal nerve subsequently bifurcates into superficial and deep peroneal nerves

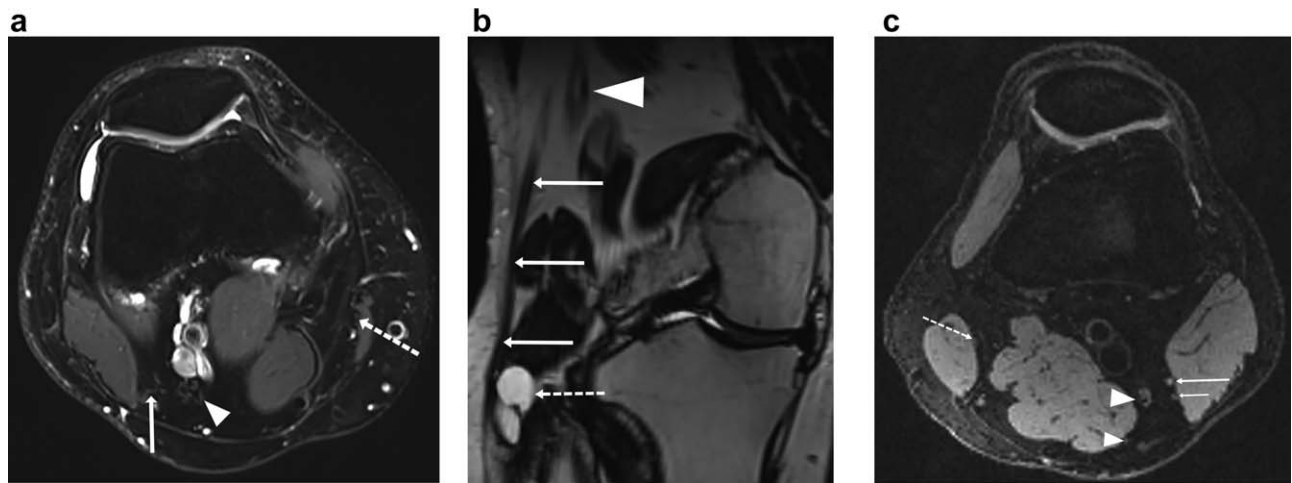


FIGURE 8: Dedicated knee neurography with SPAIR, SPACE, and DW-PSIF sequences. On this axial SPAIR (TR/TE: 3600/146 msec) image just below the sciatic bifurcation (a), there is homogenous fat saturation and high resolution, which allows visualization of the tibial (arrowhead) and common peroneal nerves (solid arrow) within the popliteal fossa as well as fascicles of the saphenous nerve just deep to the sartorius muscle at this level (dashed arrow). On an oblique coronal MPR T_2 -weighted SPACE image (TR/TE: 1200/136 msec) (b) the common peroneal nerve (straight arrows) can be followed from the bifurcation of the sciatic from the tibial nerves (arrowhead) all the way to the head of the fibula, where there is mass effect on the nerve from an adjacent ganglion cyst (dashed arrow). A DW-PSIF (TR/TE 11.5/4.5 msec, flip angle 30° , diffusion moment 85 mT/m*ms) axial image (c) demonstrates saturated flow within vessels which are now hypointense, allowing easier differentiation from nerves; the tibial (large arrowhead), common peroneal (large solid arrow), saphenous (dashed arrow), medial sural cutaneous (small arrowhead), and lateral sural cutaneous (small solid arrow) nerves are all visible.

at the level of the fibular neck, and is the most frequently abnormal nerve in the lower extremity due to its superficial location.⁶² The tibial nerve is infrequently compressed by a fibrous ridge along the superior aspect of the soleus muscle, sometimes referred to as soleus sling syndrome.⁶³ The sural and saphenous nerves can be visualized near the knee adjacent to the lesser saphenous and greater saphenous veins, respectively.

The increased signal generated by 3T machines is preferable for depicting the small nerves of the knee,⁶⁴ although if metal is present in the knee then using a 1.5T machine is preferable. Ideally the images should be obtained with as small a field of view to the area of suspected abnormality so that high-resolution images of the area in question can be generated.⁶⁵ T_1 -weighted sequences can demonstrate the small nerve fascicles of the major nerves at the knee. T_2 -weighted fat-suppressed images are essential for demonstrating the mild changes in T_2 signal within abnormal nerves. Fatty atrophy or edema from denervation can also be seen on axial T_1 - and T_2 -weighted images, respectively. These T_1 - and T_2 -weighted images are best obtained in the axial plane along the short axis of the nerves; obtaining an additional sequence in the orthogonal plane such as a coronal PD can be helpful for excluding other abnormalities in the knee that may mimic a nerve abnormality.⁶⁶ Evaluation for T_2 -weighted signal changes is complicated by the fact that nerves are subject to the magic angle phenomenon, which can falsely elevate signal when the structure runs at an angle with respect to the primary magnetic gradient, and unlike tendons this artifact can persist even on long TE images.⁶²

Spectral adiabatic inversion recovery (SPAIR) sequences are particularly helpful for this purpose in extremities such as the knee (Fig. 8a), with STIR utilized as a fallback if fat suppression remains poor. SPAIR sequences provide fat saturation with a higher spatial resolution than possible with STIR images, but with more homogenous fat saturation than typically seen with chemical fat-saturated images.⁶⁷ Intravenous contrast is generally unnecessary for standard neurography; however, it may be performed in postoperative cases or with suspicion for infection or tumor. Postcontrast images can be obtained with conventional T_1 -weighted fat sat sequences or VIBE (volume interpolated breath-hold examination) sequences if higher-resolution images are desired with the capability for 3D multiplanar reconstruction.⁶⁶

Specialized 3D sequences with isotropic voxels such as the SPACE (sampling perfection with application optimized contrast using varying flip angle evolutions) sequence are helpful for providing high resolution, thin section images that can undergo multiplanar reconstruction into any desirable plane (Fig. 8b). Most types of image contrast can be obtained with SPACE imaging; in the knee SPAIR has been a popular choice.⁶⁸ 3D maximum intensity projection (MIP) images can be produced from SPACE sequences as well. 3D DW-PSIF (diffusion-weighted reversed fast imaging in steady-state free precession) images can be used to suppress blood flow in surrounding vessels (Fig. 8c), thus aiding in the differentiation of nerves from blood vessels, as they typically lie adjacent to one another and are of similar signal intensity on other sequences.⁶⁷ DW-PSIF can help to increase certainty in nerve identification, particularly in

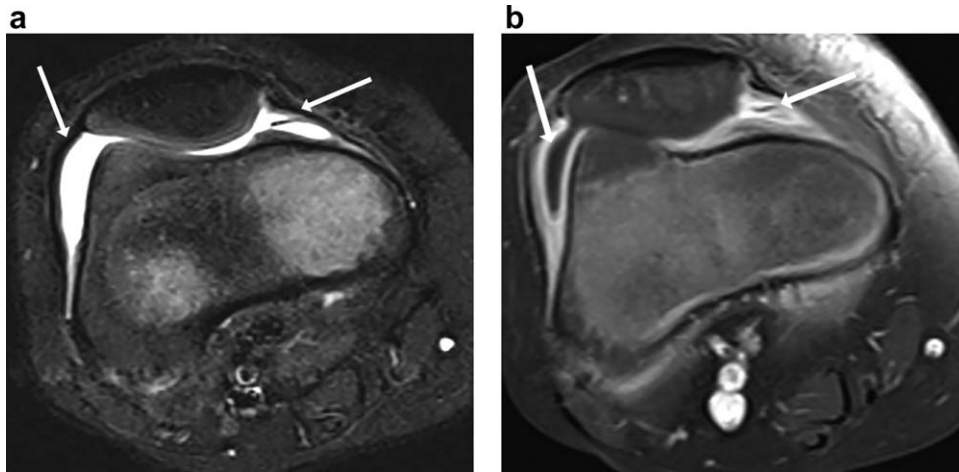


FIGURE 9: This axial STIR (TR/TE/TI: 3000/34/220 msec) image in a pediatric patient (a) demonstrates hyperintense signal in the joint which could be from synovitis or effusion. On an axial T_1 -weighted (TR/TE: 431/10 msec) fat-suppressed postcontrast image (b) most of the signal is now seen to be from thick enhancing synovitis, while a small amount of T_1 hypointense fluid is noted within the joint as well.

peripheral nerves in the extremities.⁶⁹ Although these more advanced techniques can be helpful in some situations, many institutions still rely primarily on conventional T_1 - and T_2 -weighted sequences for nerve evaluation.⁶² Diffusion tensor imaging (DTI) is a yet more advanced technique that utilizes the restricted diffusion of water in anisotropic nerves to map axonal fiber tracts and also provide quantitative information of the ADC.⁶² ADC is typically increased in pathologic conditions and decreased when nerves are regenerating after an insult.

Synovitis/Infection

Synovitis is a nonspecific reaction of the synovium which can happen with any cause of synovial inflammation, ranging from osteoarthritis to septic arthritis. The fibrous joint capsule is seen as T_1/T_2 hypointense signal along the margin of the joint, but the normal synovial lining is poorly seen by MRI, as it is typically only a few cell layers thick.⁷⁰ Evaluation for synovitis is possible on conventional sequences, primarily T_2 -weighted images with STIR sequences or T_2 -weighted chemical fat saturation. T_2 hyperintense signal in the joint may be secondary to joint effusion or synovitis, which frequently coexist. Slight relative T_2 hypointensity compared to the joint fluid or a frond-like appearance is suggestive of synovitis; adjustment of window and levels setting at the PACS workstation can help to make this distinction.⁷¹

Contrast-enhanced, fat-saturated images are best for evaluating the extent and degree of synovitis. The baseline degree of contrast enhancement in the synovium is somewhat variable⁷²; however, the presence of abundant enhancement in a frond-like pattern is consistent with synovitis. Intravenous contrast allows for distinction between the T_2 hyperintensity of joint fluid and thickened synovium (Fig. 9). The timing of imaging after contrast administration is

critical, as synovium avidly takes up contrast within the first 30–60 seconds after administration, but contrast will eventually diffuse into the joint after ~15 minutes, in which case joint effusion may enhance as well.⁷⁰ Some have utilized dynamic contrast-enhanced MRI where rheumatologic disorders have an aggressive contrast enhancement pattern with high early uptake and rapid washout, similar to tumors elsewhere in the body.⁷³ Time–intensity curves generated from dynamic contrast-enhanced imaging may be helpful for grading synovitis extent; however, this is currently limited mostly to research purposes.⁷⁴ Recent data suggests that diffusion-weighted imaging may be of benefit in distinguishing synovitis from joint effusion in patients who cannot receive contrast.⁷⁵

Pigmented villonodular synovitis (PVNS) is a common cause of knee synovitis, and has fairly specific imaging findings, given its unique pathology. T_2 hypointensity within the joint is an atypical finding, given that joint effusion and synovitis are both usually T_2 hyperintense. However, the differential diagnosis of T_2 hypointensity in the joint still remains broad, including other entities such as gout and amyloid. The presence of gradient susceptibility blooming on a gradient echo T_2^* image is compatible with hemosiderin from either PVNS or prior hemarthrosis,⁷⁶ thus adding a gradient echo T_2^* image (Fig. 10) can limit the differential diagnosis.

Characteristics of osteomyelitis include T_1 hypointensity, T_2 hyperintensity, and contrast enhancement within the medullary bone, often adjacent to a soft-tissue ulceration or focus of infection. However, isolated T_2 hyperintensity and enhancement within the medullary bone is a nonspecific finding that can also be seen with reactive changes in the bone from adjacent infection, as opposed to true infection within the bone itself. T_1 marrow hypointensity, particularly in a confluent pattern, is a much more specific finding

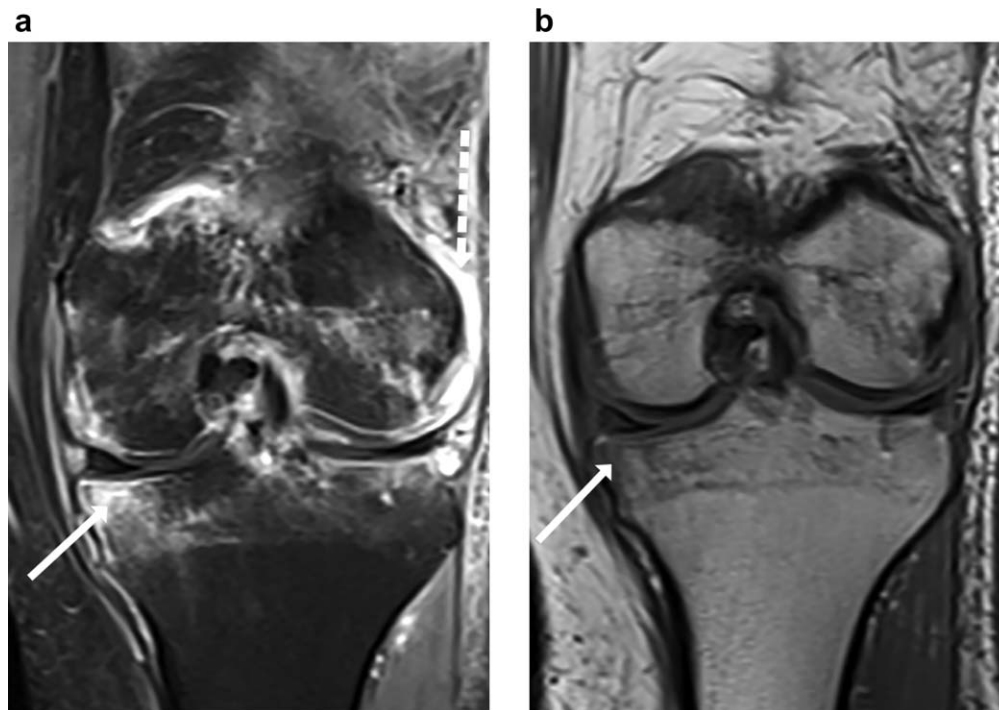


FIGURE 10: This coronal T_1 fat-suppressed postcontrast (TR/TE: 894/17 msec) image (a) from a patient with known septic arthritis demonstrates enhancement of the synovium (dotted arrow), with enhancement in the medial tibial plateau (solid arrow) that could be secondary to either underlying osteomyelitis or reactive changes secondary to the adjacent infection. The presence of focal T_1 hypointensity (solid arrow) within the medial tibial plateau on a T_1 (TR/TE: 779/16 msec)-weighted image (b) confirms the diagnosis of osteomyelitis.

of osteomyelitis (Fig. 11)⁷⁷; thus, obtaining T_1 -weighted images is critical.

The popliteal artery typically lies between the two heads of the gastrocnemius muscle, but alterations in this relationship can lead to vascular symptoms in the lower extremity secondary to popliteal artery entrapment syndrome. These patients are typically young and male and present with intermittent calf claudication.⁷⁸ Traditionally, digital subtraction angiography has been the preferred mode of evaluation for popliteal artery entrapment. However, MRI has demonstrated its utility, since it can demonstrate the entrapment utilizing MRA sequences as well as the underlying muscle abnormality causing the vascular abnormality.⁷⁹ A dedicated protocol is necessary for evaluation of popliteal artery entrapment, including conventional T_1 - and T_2 -weighted fat-suppressed axial images to demonstrate the underlying muscle abnormality (Fig. 12a) as well as time-of-flight MRA images in both plantar flexion and dorsiflexion (Fig. 12b). The popliteal artery narrowing seen with entrapment may be positional; thus, imaging in both dorsiflexion and plantarflexion is required.⁷⁹

3T Field Strength MRI

1.5T imaging has served as the backbone of knee MRI evaluation, and remains acceptable for diagnostic purposes. However, 3T imaging does have its advantages, as the higher SNR allows for either faster scanning or higher-resolution images.⁸⁰ Potential drawbacks to 3T scanning include

increased chemical shift, susceptibility artifact, and increased radiofrequency specific absorption rate (SAR) to the patient.⁸⁰ 3T is particularly useful in nerve imaging or if

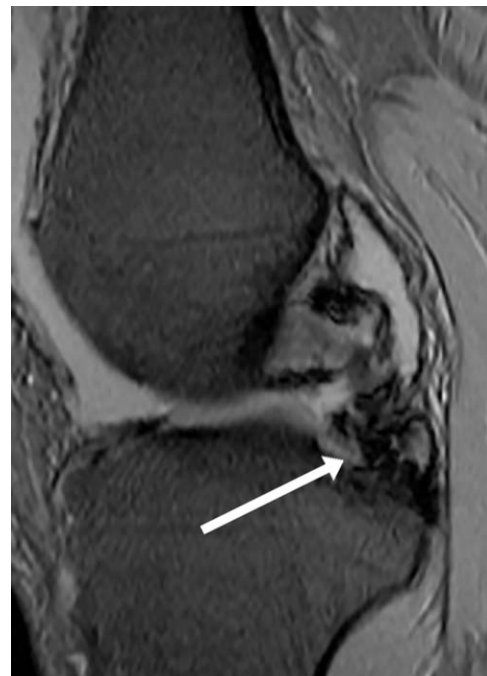


FIGURE 11: This sagittal gradient echo T_2 image (TR/TE: 566/9.5 msec, flip angle 30°) demonstrates hypointense blooming signal along the posterior cruciate ligament, consistent with PVNS. Without the gradient echo image, a more extensive differential diagnosis would be necessary.

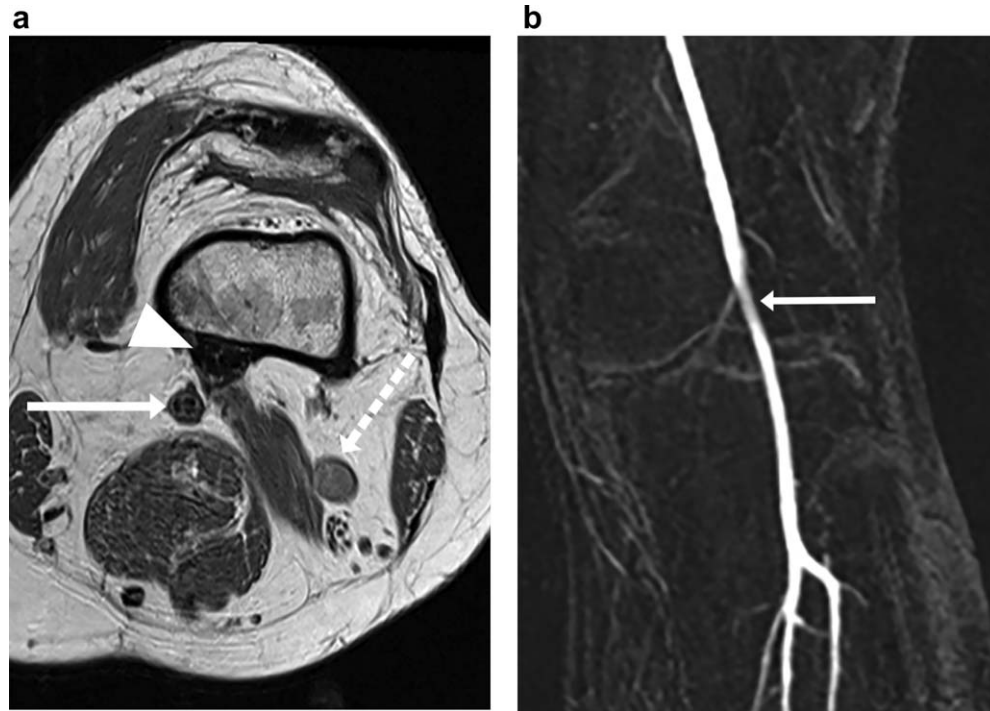


FIGURE 12: This conventional T_1 -weighted axial image (TR/TE: 619/13 msec) (a) demonstrates an anomalous origin of the medial gastrocnemius (arrowhead), which lies between the popliteal artery (straight arrow) and popliteal vein (dotted arrow), an arrangement that can predispose to popliteal artery entrapment syndrome. A coronal TWIST time-of-flight MRA subtraction MIP image from a different patient (b) shows slight narrowing of the popliteal artery with plantarflexion positioning (straight arrow), thought to be secondary to muscular hypertrophy of the gastrocnemius in a young patient; no corresponding narrowing was seen on dorsiflexion images.

3D imaging is planned, but should specifically be avoided if a patient known to have a metallic implant in the knee is to be imaged. Imaging protocols must be specifically tailored for 3T magnets, as simply transposing optimized 1.5T protocols to a 3T magnet may result in poor images or prolonged imaging time.⁸⁰ Studies have demonstrated conventional 3T images to be at least as good as 1.5T images for evaluating the menisci.⁸¹

3D Sequences

Traditionally, the bulk of MRI evaluation for internal derangement of the knee has consisted of obtaining 2D images of different weighting in different planes. However, 2D sequences consist of relatively thick sections with an interslice gap, thus potentially leading to volume averaging artifacts.⁵¹ 3D sequences, such as SPACE on Siemens scanners and CUBE on GE scanners, may have a longer acquisition time than conventional sequences, but the ability to reconstruct images in any plane allows one to potentially replace multiple 2D images. Recent research has suggested that the use of limited 3D sequences with subsequent reconstruction in different planes can perform similarly to traditional 2D imaging in evaluation of the meniscus, ligaments, cartilage, and bone marrow.^{51,82,83} 3D images may be particularly beneficial for visualizing areas that have traditionally been difficult to assess on 2D images, particularly the

meniscal roots and trochlear cartilage.⁸⁴ Current clinical utilization of 3D imaging is primarily for cartilage and nerve evaluation, but with further research additional applications may come to light.

Ultrashort TE

Structures such as the menisci, ligaments, tendons, and cortical bone in the knee all demonstrate hypointense signal on conventional T_1 - and T_2 -weighted images because the T_2 relaxation time of the tissues is shorter than the shortest possible TE achievable with conventional techniques.⁸⁵ Ultrashort echo time (UTE) images utilize echo times that are at least 50 times shorter than in conventional images,⁸⁶ which allows for increased signal within these typically dark structures and more possibilities for contrast manipulation. UTE images can be obtained with either 2D or 3D techniques, potentially with the addition of fat suppression or gadolinium intravenous contrast.⁸⁵ Contrast between structures can be adjusted based on changes in the flip angle, TE, or repetition time (TR), allowing differentiation in signal between tendons and the fibrocartilage within the meniscus (Fig. 13a). Images are often acquired using a dual echo pulse sequence, yielding one image with UTE (TE <0.1 msec) and another with a longer, more conventional echo time (TE >2 msec).⁸⁷ Subtracting the second image from the first can also alter contrast between structures in the

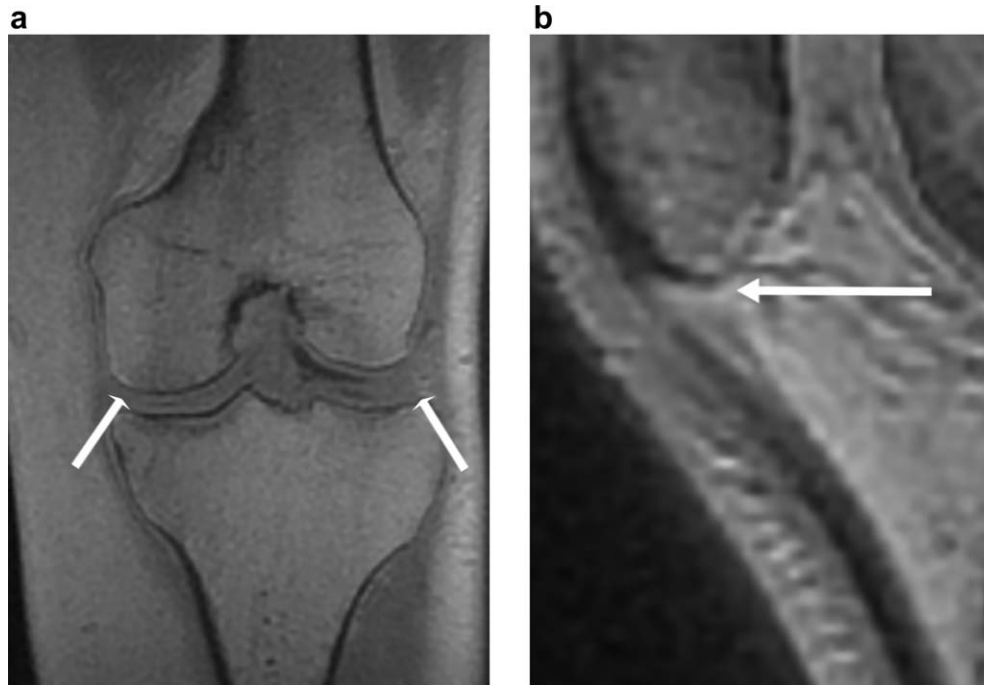


FIGURE 13: 3D UTE imaging of knee menisci (TR/TE: 6/0.08 msec, flip angle 5°, first echo of dual echo acquisition) demonstrates diffusely hyperintense signal within the menisci (arrows) on this coronal reconstructed image (a); the menisci are typically hypointense on all conventional sequences. Sagittal reconstruction of the second echo from UTE image acquisition (TR/TE: 6/2.5 msec, flip angle 5°), (b) demonstrates intermediate signal near the insertion of the patellar tendon, thus allowing identification of the fibrocartilaginous entheses (solid arrow) separate from the cortical bone and remainder of the tendon.

knee.⁸⁸ Quantitative techniques including T_2 and T_1 rho mapping can be combined with UTE acquisition to assess the cartilage and menisci.^{85,89} UTE MRI has been utilized to study the fibrous entheses at tendon insertion on bone (Fig. 13b); typically, the enthesis is of similar signal intensity as tendon and cortical bone but with UTE the contrast between the fibrous entheses and the adjacent structures can be achieved.⁹⁰ Evaluation of meniscal tears using UTE remains in its infancy, but early findings have suggested that tears appear as linear black signal superimposed on a bright meniscal background on subtraction images, and gadolinium can be utilized to differentiate the vascularized from unvascularized portions of the meniscus.⁸⁶ Currently, these techniques are utilized for research purposes and have yet to find widespread clinical usage.

UTE sequences have also been used to obtain quantitative images of the structural elements in the knee based on differences in T_2^* relaxation time, sometimes referred to as UTE mapping.⁹¹ The technology has been studied for cartilage imaging, with higher T_2^* values found in normal cartilage and lower values in degenerated cartilage. Differences in cartilage organization can even be detected in the deeper cartilage layers serving as a potential advantage compared to conventional T_2 mapping,⁹² and the sequence can potentially be used with standard clinical scanners and knee coils.⁹³ UTE mapping can potentially show a decrease in T_2^* values relative to healthy menisci in patients with subclinical meniscal injury, but without evidence of intrasubstance meniscal

denegation or a tear on conventional sequences.⁹⁴ A variety of different parameters can be quantitatively assessed in the cortical bone using UTE sequences, but the mapping of cortical bone water (including total, bound, and free water) likely has the greatest potential for evaluating osteoporotic fracture risk. Significant differences have been detected in cortical bone water between patients with renal osteodystrophy, postmenopausal patients, and premenopausal patients greater than the differences seen in the same patients groups when using standard dual x-ray absorptiometry (DEXA).⁹⁵ There is also evidence that quantitative UTE techniques may be able to detect early degeneration in tendons.⁹⁶

In conclusion, MRI provides a comprehensive evaluation of soft tissue and osseous structures, allowing for accurate assessment of knee pathology. MR is useful for the diagnosis of meniscal and cruciate injuries, which are very common reasons to perform orthopedic surgery. Advancements in MRI continually improve the value and application of knee MR for the assessment of postoperative change, tumors, nerves, cartilage defects, and synovitis/infection. Development of sequences that deal with metal artifact reduction and ultrashort TE continue to bring MRI of the knee to new levels.

References

1. Oei EHG, Nikken JJ, Verstijnen ACM, Hunink MGM. Radiology MR imaging of the menisci and cruciate ligaments: A systematic review. *Radiology* 2000;837–848.

2. De Smet AA, Graf BK, Rosas HG. MR imaging-based diagnosis and classification of meniscal tears. *RadioGraphics* 2014;34:981–999.
3. Rosas HG. Magnetic resonance imaging of the meniscus knee tear magnetic resonance imaging MRI. *Magn Reson Imaging Clin NA* 2016;22:493–516.
4. De Smet AA. Tears on knee MRI. *Am J Roentgenol* 2012;199:481–499.
5. Harper KW, Helms CA, Lambert HS, et al. Radial meniscal tears: significance, incidence, and MR appearance. 2005:1429–1434.
6. De Smet AA, Graf BK, Munoz A. Association of parameniscal cysts with underlying meniscal tears as identified on MRI and arthroscopy. *AJR Am J Roentgenol* 2011;180–186.
7. Tuckman G, Miller W, Frifits H, Rozansky M. Pictorial essay radial tears of the menisci: MR findings. *Am J Roentgenol* 1994;163:395–400.
8. Mcknight A, Southgate J, Price A. Meniscal tears with displaced fragments: common patterns on magnetic resonance imaging. *Skeletal Radiol* 2010:279–283.
9. De Smet AA, Blankenbaker DG, Kijowski R, Graf BK, Shinki K. MR diagnosis of posterior root tears of the lateral meniscus using arthroscopy as the reference standard. *Am J Roentgenol* 2009;192:480–486.
10. Lee S, Jee W, Kim J. Radial Tear of the Medial Mensical Root: Reliability and Accuracy of MRI for Diagnosis *Am J Roentgenol*. 2008; 191:81–85.
11. Isotropic CW, Jung J, Jee W, et al. Meniscal tear configurations. *Am J Roentgenol* 2012;198:173–180.
12. Naraghi A, White LM. MR imaging of cruciate ligaments. *Magn Reson Imaging Clin NA* 2016;22:557–580.
13. Kijowski R, Lee KS, Muroz A, et al. Short-term clinical importance of osseous injuries diagnosed at MR imaging in patients with anterior cruciate ligament tear 1. *Am J Roentgenol* 2012;264:531–541.
14. Paper AR. Partial tears of the anterior cruciate ligament: diagnosis and treatment. *Am J Orthop*. 2011;40:2–7.
15. Ng AWH, Griffith JF, Hung EHY, Law KY, Yung PSH. MRI diagnosis of ACL bundle tears: value of oblique axial imaging. *Skeletal Radiol* 2013:209–217.
16. Park HJ, Kim SS, Lee SY, Park NK, Ahn JH, et al. Comparison Between Arthroscopic Findings and 1.5-T and 3-T MRI of Oblique Coronal and Sagittal Planes of the Knee for Evaluation of Selective Bundle Injury of the Anterior Cruciate Ligament *Am J Roentgenol*. 2014;203:199–206.
17. Kijowski R, Davis KW, Woods MA, Lindstrom MJ, De Smet AA, et al. Knee joint: comprehensive assessment with 3D isotropic resolution fast spin-echo MR imaging — diagnostic performance compared with that of conventional MR imaging at 3.0 T. *Radiology* 2009;252:486–495.
18. Rodriguez W, Vinson EN, Helms CA, Toth AP. MRI appearance of posterior cruciate ligament tears. *Am J Roentgenol* 2008;191:155–159.
19. Davis KW, Tuite MJ. MR imaging of the postoperative meniscus of the knee. *Semin Musculoskelet Radiol* 2002;6:35–45.
20. Ugas MA, Huynh BH, Fox MG, Patrie JT, Gaskin CM. MR arthrography: impact of steroids, local anesthetics, and iodinated contrast material on gadolinium signal intensity in phantoms at 1.5 and 3.0 T. *Radiology* 2014;272:475–483.
21. White LM, Schweitzer ME, Weishaupt D, Kramer J, Davis A, Marks PH. Diagnosis of recurrent meniscal tears: prospective evaluation of conventional MR imaging, indirect MR arthrography, and direct MR arthrography. *Radiology* 2002;222:421–429.
22. Deniz C, Asim C, Elverici E, Sakman B, Yüksel E, Akbulut O. Evaluation of postoperative menisci with MR arthrography and routine conventional MRI. *Clinical Imaging* 2008;32:212–219.
23. Magee T, Shapiro M, Rodriguez J, Williams D. MR arthrography of postoperative knee: for which patients is it useful? *Radiology* 2003; 229:159–163.
24. De Smet AA. MR imaging and MR arthrography for diagnosis of recurrent tears in the postoperative meniscus. *Seminars in Musculoskeletal Radiology* 2005;9:116–124.
25. Magee T. Accuracy of 3-Tesla MR and MR arthrography in diagnosis of meniscal retear in the post-operative knee. *Skeletal Radiol* 2014;43: 1057–1064.
26. Boutin RD, Fritz RC, Marder RA. Magnetic resonance imaging of the postoperative meniscus. *Magn Reson Imaging Clin NA* 2016;22: 517–555.
27. Fayad LM, Jacobs MA, Wang X, Carrino JA, Bluemke DA. Musculoskeletal tumors: how to use anatomic, functional, and metabolic MR techniques. *Radiology* 2012;265:340–356.
28. Vogler JB, Murphy WA. Bone marrow imaging. *Radiology* 1988;168: 679–693.
29. Vanel D, Shapeero LG, De Baere T, et al. MR imaging in the follow-up of malignant and aggressive soft-tissue tumors: results of 511 examinations. *Radiology* 1994;190:263–268.
30. Zajick DC, Morrison WB, Schweitzer ME, Parellada JA, Carrino JA. Benign and malignant processes: normal values and differentiation with chemical shift MR imaging in vertebral marrow. *Radiology* 2005;237:590–596.
31. Vilanova JC, Baleato-Gonzalez S, Romero MJ, Carrascoso-Arranz J, Luna A. Assessment of musculoskeletal malignancies with functional MR imaging. *Magn Reson Imaging Clin N Am* 2016;24:239–259.
32. Genovese E, Cania, Rizzo S, Angeretti MG, Leonardi A, Fugazzola C. Comparison between MRI with spin-echo echo-planar diffusion-weighted sequence (DWI) and histology in the diagnosis of soft-tissue tumours. *Radiol Med* 2011;116:644–656.
33. Del Grande F, Subhawong T, Weber K, Aro M, Mugera C, Fayad LM. Detection of soft-tissue sarcoma recurrence: added value of functional MR imaging techniques at 3.0 T. *Radiology* 2014;271:499–511.
34. Hayashida Y, Yakushiji T, Awai K, et al. Monitoring therapeutic responses of primary bone tumors by diffusion-weighted image: Initial results. *Eur Radiol* 2006;16:2637–2643.
35. Ma LD, Frassica FJ, McCarthy EF, et al. Benign and malignant musculoskeletal masses: MR imaging differentiation with rim-to-center differential enhancement ratios. *Radiology* 1997;202:739–744.
36. van Rijswijk CSP, Geirnaerd MJA, Hogendoorn PCW, et al. Soft-tissue tumors: value of static and dynamic gadopentetate dimeglumine-enhanced MR imaging in prediction of malignancy. *Radiology* 2004; 233:493–502.
37. van der Woude HJ, Verstraete KL, Hogendoorn PC, Taminiau AH, Hermans J, Bloem JL. Musculoskeletal tumors: does fast dynamic contrast-enhanced subtraction MR imaging contribute to the characterization? *Radiology* 1998;208:821–828.
38. Fayad LM, Barker PB, Jacobs MA, et al. Characterization of musculoskeletal lesions on 3-T proton MR spectroscopy. *Am J Roentgenol* 2007;188:1513–1520.
39. Chang EY, Bae WC, Chung CB. Imaging the knee in the setting of metal hardware. *Magn Reson Imaging Clin N Am* 2014;22:765–786.
40. Dillenseger JP, Molière S, Choquet P, Goetz C, Ehlinger M, Bierry G. An illustrative review to understand and manage metal-induced artifacts in musculoskeletal MRI: a primer and updates. *Skeletal Radiol* 2016:677–688.
41. Lee M-J, Kim S, Lee S-A, et al. Overcoming artifacts from metallic orthopedic implants at high-field-strength MR imaging and multidetector CT. *Radiographics* 2007;27:791–804.
42. Lazik A, Landgraeber S, Schulte P, Kraff O, Lauenstein TC, Theysohn JM. Usefulness of metal artifact reduction with WARP technique at 1.5 and 3T MRI in imaging metal-on-metal hip resurfacings. *Skeletal Radiol* 2015:941–951.
43. Talbot BS, Weinberg EP. MR Imaging with metal-suppression sequences for evaluation of total joint arthroplasty. *Radiographics* 2016;36:209–225.
44. Koch KM, Hargreaves BA, Pauly KB, Chen W, Gold GE, King KF. Magnetic resonance imaging near metal implants. *J Magn Reson Imaging* 2010;32:773–787.
45. Rubenstein J, Li JG, Majumdar S, Henkelman RM. Image resolution and signal-to-noise ratio requirements for MR imaging of degenerative cartilage. for MR imaging. *Cartilage* 1997:1089–1096.

46. Guermazi A, Roemer FW, Alizai H, et al. State of the art: MR imaging after knee cartilage repair surgery. *Radiology* 2015;277:23–43.
47. Guermazi A, Alizai H, Crema MD, Trattinig S, Regatte RR, Roemer FW. Compositional MRI techniques for evaluation of cartilage degeneration in osteoarthritis. *Osteoarthritis Cartilage* 2015;23:1639–1653.
48. Watanabe A, Wada Y, Obata T, et al. Delayed gadolinium-enhanced MR to determine glycosaminoglycan concentration in reparative cartilage after autologous chondrocyte implantation: preliminary results. *Radiology* 2006;239:201–208.
49. Mamisch TC, Hughes T, Mosher TJ, et al. T2 star relaxation times for assessment of articular cartilage at 3T: A feasibility study. *Skeletal Radiol* 2012;41:287–292.
50. Roemer FW, Kwok CK, Hannon MJ, et al. Semiquantitative assessment of focal cartilage damage at 3T MRI: A comparative study of dual echo at steady state (DESS) and intermediate-weighted (IW) fat-suppressed fast spin echo sequences. *Eur J Radiol* 2011;80:126–131.
51. Kijowski R, Davis KW, Woods MA, et al. Knee joint: comprehensive assessment with 3D isotropic resolution fast spin-echo MR imaging—diagnostic performance compared with that of conventional MR imaging at 3.0 T. *Radiology* 2009;252:486–495.
52. Mohr A. The value of water-excitation 3D FLASH and fat-saturated PDw TSE MR imaging for detecting and grading articular cartilage lesions of the knee. *Skeletal Radiol* 2003;32:396–402.
53. Crema MD, Roemer FW, Marra MD, et al. Articular cartilage in the knee: current MR imaging techniques and applications in clinical practice and research. *Radiographics* 2011;31:37–61.
54. Mosher TJ, Smith H, Dardzinski BJ, Schmithorst VJ, Smith MB. MR imaging and T2 mapping of femoral cartilage: in vivo determination of the magic angle effect using T-mapping of femoral cartilage. *Am J Roentgenol* 2001;177:665–659.
55. Dunn TC, Lu Y, Jin H, Ries MD, Majumdar S. T2 relaxation time of cartilage at MR imaging: comparison with severity of knee osteoarthritis. *Radiology* 2004;232:592–598.
56. Madelin G, Lee JS, Regatte RR, Jerschow A. Sodium MRI: Methods and applications. *Prog Nucl Magn Reson Spectrosc* 2014;79:14–47.
57. Holtzman D, Theologis A, Carballido-Gamio J, Majumdar S, Li X, Benjamin C. T(1ρ) and T(2) quantitative magnetic resonance imaging analysis of cartilage regeneration following microfracture and mosaicplasty cartilage resurfacing procedure. *J Magn Reson Imaging* 2010;32:914–923.
58. Duvvuri U, Charagundla SR, Kudchodkar SB, et al. Human knee: in vivo T1(ρ)-weighted MR imaging at 1.5 T—preliminary experience. *Radiology* 2001;220:822–826.
59. Theologis AA, Schairer WW, Carballido-Gamio J, Majumdar S, Li X, Ma CB. Longitudinal analysis of T 1 and T 2 quantitative MRI of knee cartilage laminar organization following microfracture surgery. *Knee* 2012;19:652–657.
60. Welsch GH, Trattinig S, Domayer S, Marlovits S, White LM, Mamisch TC. Multimodal approach in the use of clinical scoring, morphological MRI and biochemical T2-mapping and diffusion-weighted imaging in their ability to assess differences between cartilage repair tissue after microfracture therapy and matrix-associated autologous chondrocyte transplantation: a pilot study. *Osteoarthritis Cartilage* 2009;17:1219–1227.
61. Damarey B, Demondion X, Wavreille G, Pansini V, Balbi V, Cotten A. Imaging of the nerves of the knee region. *Eur J Radiol* 2013;82:27–37.
62. Burge AJ, Gold SL, Kuong S, Potter HG. High-resolution magnetic resonance imaging of the lower extremity nerves. *Neuroimaging Clin N Am* 2014;24:151–170.
63. Chhabra A, Williams EH, Subhawong TK, et al. MR neurography findings of soleal sling entrapment. *Am J Roentgenol* 2011;196:290–297.
64. Cejas C, Aguilar M, Falcon L, Caneco N, Acuna MC. High resolution (3T) magnetic resonance neurography of the sciatic nerve. *Radiologia* 2012;56:107–117.
65. Carpenter EL, Bencardino JT. Focus on advanced magnetic resonance techniques in clinical practice: magnetic resonance neurography. *Radiol Clin North Am* 2015;53:513–529.
66. Chhabra A, Flammang A, Padua A, Carrino JA, Andreisek G. Magnetic resonance neurography. Technical considerations. *Neuroimaging Clin N Am* 2014;24:67–78.
67. Chalian M, Soldatos T, Faridian-Aragh N, et al. 3T magnetic resonance neurography of tibial nerve pathologies. *J Neuroimaging* 2013;23:296–310.
68. Chhabra A, Lee PP, Bizzell C, Soldatos T. 3 Tesla MR neurography — Technique, interpretation, and pitfalls. *Skeletal Radiol* 2011;40:1249–1260.
69. Chhabra A, Soldatos T, Subhawong TK, et al. The application of three-dimensional diffusion-weighted PSIF technique in peripheral nerve imaging of the distal extremities. *J Magn Reson Imaging* 2011;34:962–967.
70. Chung CB, Boucher R, Resnick D. MR Imaging of synovial disorders of the knee. *Semin Musculoskelet Radiol* 2009;13:303–325.
71. Flemming DJ, Hash TW, Bernard SA, Brian PS. MR imaging assessment of arthritis of the knee. *Magn Reson Imaging Clin N Am* 2014;22:703–724.
72. Boegård T, Johansson A, Rudling O, Petersson I, Forslind K, Jonsson K. Gadolinium-DTPA-enhanced MR imaging in asymptomatic knees. *Acta Radiol* 1996;37:877–882.
73. van de Sande MGH, van der Leij C, Lavini C, Wijbrandts CA, Maas M, Tak PP. Characteristics of synovial inflammation in early arthritis analysed by pixel-by-pixel time-intensity curve shape analysis. *Rheumatology* 2012;51:1240–1245.
74. Hayashi D, Roemer FW, Katur A, et al. Imaging of synovitis in osteoarthritis: current status and outlook. *Semin Arthritis Rheum* 2011;41:116–130.
75. Li X, Liu X, Du X, Ye Z. Diffusion-weighted MR imaging for assessing synovitis of wrist and hand in patients with rheumatoid arthritis: A feasibility study. *Magn Reson Imaging* 2014;32:350–353.
76. Wadhwa V, Cho G, Moore D, Pezeshk P, Coyner K, Chhabra A. T2 black lesions on routine knee MRI: differential considerations. *Eur Radiol* 2016;26:2387–2399.
77. Johnson PW, Collins MS, Wenger DE. Diagnostic utility of T1-weighted MRI characteristics in evaluation of osteomyelitis of the foot. *Am J Roentgenol* 2009;192:96–100.
78. Wright LB, Jean MW, Cruz CP, et al. Popliteal artery disease: diagnosis and treatment. *Radiographics* 2004;24:467–479.
79. Hai Z, Guangrui S, Yuan Z, et al. CT angiography and MRI in patients with popliteal artery entrapment syndrome. *Am J Roentgenol* 2008;191:1760–1766.
80. Bolog N, Nanz D, Weishaupt D. Musculoskeletal MR imaging at 3.0T: Current status and future perspectives. *Eur Radiol* 2006;16:1298–1307.
81. Sampson MJ, Jackson MP, Moran CJ, Moran R, Eustace SJ, Shine S. Three Tesla MRI for the diagnosis of meniscal and anterior cruciate ligament pathology: a comparison to arthroscopic findings. *Clin Radiol* 2008;63:1106–1111.
82. Jung JY, Yoon YCh, Kim HR, Choe B-K, Wang JH, Jung JY. Knee derangements: comparison of isotropic 3D fast spin-echo, isotropic 3D balanced fast field-echo, and conventional 2D fast spin-echo MR imaging. *Radiology* 2013;268:802–813.
83. Kudo H, Inaoka T, Kitamura N, et al. Clinical value of routine use of thin-section 3D MRI using 3D FSE sequences with a variable flip angle technique for internal derangements of the knee joint at 3T. *Magn Reson Imaging* 2013;31:1309–1317.
84. Notohamprodo M, Horng A, Kuschel B, et al. 3D-imaging of the knee with an optimized 3D-FSE-sequence and a 15-channel knee-coil. *Eur J Radiol* 2012;81:3441–3449.
85. Bae WC, Du J, Bydder GM, Chung CB. Conventional and ultrashort time-to-echo magnetic resonance imaging of articular cartilage, meniscus, and intervertebral disk. *Top Magn Reson Imaging* 2010;21:275–289.

86. Gatehouse PD, Thomas RW, Robson MD, Hamilton G, Herlihy AH, Bydder GM. Magnetic resonance imaging of the knee with ultrashort TE pulse sequences. *Magn Reson Imaging* 2004;22:1061–1067.
87. Rahmer J, Blume U, Bornert P. Selective 3D ultrashort TE imaging: Comparison of “dual-echo” acquisition and magnetization preparation for improving short-T2 contrast. *Magn Reson Mater Phys Biol Med* 2007;20:83–92.
88. Lee YH, Kim S, Song H-T, Kim I, Suh J-S. Weighted subtraction in 3D ultrashort echo time (UTE) imaging for visualization of short T2 tissues of the knee. *Acta Radiol* 2014;55:454–461.
89. Sneag DB, Shah P, Koff MF, Lim WY, Rodeo SA, Potter HG. Quantitative ultrashort echo time magnetic resonance imaging evaluation of postoperative menisci: a pilot study. *HSS J* 2015;11:123–129.
90. Benjamin M, Bydder GM. Magnetic resonance imaging of entheses using Ultrashort TE (UTE) pulse sequences. *J Magn Reson Imaging* 2007;25:381–389.
91. Chang EY, Du J, Chung CB. UTE imaging in the musculoskeletal system. *J Magn Reson Imaging* 2015;41:870–883.
92. Williams A, Qian Y, Bear D, Chu CR. Assessing degeneration of human articular cartilage with ultra-short echo time (UTE) T2* mapping. *Osteoarthritis Cartilage* 2010;18:539–546.
93. Williams A, Qian Y, Chu CR. UTE-T2* mapping of human articular cartilage in vivo: A repeatability assessment. *Osteoarthritis Cartilage* 2011;19:84–88.
94. Williams A, Qian Y, Golla S, Chu CR. UTE-T2* mapping detects sub-clinical meniscus injury after anterior cruciate ligament tear. *Osteoarthritis Cartilage* 2012;20:486–494.
95. Techawiboonwong A, Song HK, Leonard MB, Wehrli FW. Cortical bone water: in vivo quantification with ultrashort echo-time MR imaging. *Radiology* 2008;248:824–833.
96. Juras V, Zbyn S, Pressl C, et al. Regional variations of T2* in healthy and pathologic achilles tendon in vivo at 7 Tesla: Preliminary results. *Magn Reson Med* 2012;68:1607–1613.